Ecological Indicators 181 (2025) 114388

Contents lists available at ScienceDirect

Ecological Indicators

journal homepage: www.elsevier.com/locate/ecolind

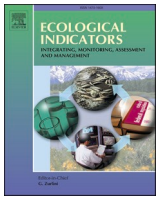

An indicator framework for assessing forest ecosystem productivity resilience and transition risks under climate change

Yingshuo Lyu [a,b], Xi Zheng [a,*], Han Wang [b], Teng Liu [c,d], Chutong Chao [a], Xiaoyang Ou [a]

[a] School of Landscape Architecture, Beijing Forestry University, Beijing 100083, China
[b] Department of Earth System Science, Ministry of Education Key Laboratory for Earth System Modeling, Institute for Global Change Studies, Tsinghua University, Beijing 100084, China
[c] School of Systems Science and Institute of Nonequilibrium Systems, Beijing Normal University, Beijing 100875, China
[d] Earth System Modelling, School of Engineering and Design, Technical University of Munich, Munich 85748, Germany

ARTICLE INFO

Keywords:
Ecosystem productivity resilience (EPR)
Critical slowing down (CSD) metrics
Climatic water availability
State transitions
Forest ecosystem
Adaptive forest management
Spatial resilience assessment

ABSTRACT

Climate variability is increasingly threatening forest ecosystem functioning and carbon sink stability, reducing resilience and triggering abrupt state transitions. Ecosystem productivity resilience (EPR)—the ability to maintain and recover carbon sequestration function under disturbance—is a key dimension of functional resilience. Declining EPR often precedes functional anomalies and signals increased risk of critical transitions. However, previous studies have largely focused on temporal trends and lack spatially explicit methods for assessing resilience states and transition risks. We develop a composite indicator framework to quantify EPR variation using critical slowing down (CSD) metrics derived from gross primary production (GPP) time series. By integrating structure and process characteristics, we identify EPR states and potential transitions under climate change. Applied across China from 2000 to 2018, the framework reveals that 57.47% of forests experienced an EPR decline, primarily driven by climatic water availability. Coniferous-broadleaf forests in the temperate zone experienced the most severe abrupt declines under both water surplus and deficit. Reductions in EPR and productivity are statistically linked and emerge as ecosystems approach critical thresholds. Notably, 24.58% of forests have transitioned from a state of uniform stability to unstable multistability. As projected EPR degradation escalates under persistent warming, high-risk transitions increasingly cluster in boundary areas and high-vulnerability shifts toward productive lower latitudes. Our findings highlight the urgency of incorporating the EPR indicator system into resilience assessments and informing ecological adaptation management.

1. Introduction

Forests comprise 80–90 % of global plant biomass (Pan et al., 2011) and play a fundamental role in providing ecosystem services and achieving climate goals (Friedlingstein et al., 2022; McDowell et al., 2020; Reid et al., 2005). However, they are endangered by climatic stressors (such as high temperatures, increased water stress and evaporative demand) and land use-related disturbances, raising substantial concerns (Anderegg et al., 2015; Hoek van Dijke et al., 2022; Liu et al., 2024). Among them, hydroclimatic fluctuations have been observed to accelerate forest mortality (Senf et al., 2020) and induce annual carbon fluxes of up to 2–3 gigatons (Green et al., 2019). Empirical and experimental evidence indicate that disturbances directly degrade resilience, preceding functional anomalies and ecosystem collapse (Folke et al., 2004; Gladstone-Gallagher et al., 2019; Greenwell et al., 2019; Holling, 1996; Scheffer et al., 2001). These delayed responses across ecosystem structure, processes, and functions underscore the need to prioritize long-term functional resilience over merely short-term service provision (Aguirre-Gutiérrez et al., 2022; Oliver et al., 2015).

Ecosystem productivity resilience (EPR), defined as the ability of the carbon sequestration function to withstand and recover from environmental perturbations, represents a key dimension of functional resilience. It drives ecosystem energy and carbon exchange, supports persistence and functional diversity, and sustains service provision (Cook-Patton et al., 2020; Folke et al., 2004; Poorter et al., 2016). Low-EPR forests are more susceptible to both ecosystem structure and processes destabilization (Cumming and Peterson, 2017). The “marble in a cup” conceptual model (Holling, 1996; Walker et al., 2004) illustrates

* Corresponding author.
E-mail address: zhengxi@bjfu.edu.cn (X. Zheng).

https://doi.org/10.1016/j.ecolind.2025.114388
Received 30 May 2025; Received in revised form 18 October 2025; Accepted 28 October 2025
Available online 14 November 2025

that the size of the attraction basin determines the structural stability of a system with multiple stable states, reflecting self-organizing capacity within processes (Method. S1 and Fig. S1). Far from the critical threshold, systems exhibit broad and deep basins of attraction, as well as a swift recovery rate from perturbations (Andersen et al., 2009; Scheffer and Carpenter, 2003). As tipping points are approached, the basin shrinks and the recovery rate slows, and system states become increasingly autocorrelated due to critical slowing down (CSD) (Scheffer et al., 2009). Once thresholds are crossed, disturbances may trigger frequent and abrupt fluctuations between alternative states and give rise to multiple coexisting attractors. This manifests as a self-sustained runaway multistable state, leading to permanent loss of EPR and carbon sequestration capacity, accelerating climate change and undermining biodiversity and socioeconomic systems (Bochow and Boers, 2023; Flores et al., 2024; McDowell et al., 2020; Scheffer et al., 2001). Thus, declines in EPR (Scheffer et al., 2009) and structure–process stability (Keith et al., 2023) serve as early warnings of catastrophic transition. Given escalating disturbance regimes (Flores et al., 2024; Seidl et al., 2017), monitoring EPR tipping dynamics to guide preemptive management has become increasingly urgent.

Despite its importance, large-scale assessment of EPR remains limited (Oliver et al., 2015). Growing studies infer resilience decline using CSD indicators, typically manifested as heightened temporal autocorrelation (TAC) and variance in time series (Dakos et al., 2015; Liu et al., 2023; Rietkerk et al., 2021; Scheffer et al., 2001, 2009). Lag-one autocorrelation (AR(1)) captures system memory and recovery rate, while variance reflects the magnitude of natural fluctuations (Dakos et al., 2008). However, these trend-based approaches offer limited insight into the structure–process characteristics of resilience. An indicator framework for identifying EPR states and anticipating potential transitions is still lacking.

We develop a systematic approach that combines CSD metrics with structure–process characteristics to assess EPR. First, EPR variation is estimated using CSD metrics derived from satellite-based gross primary production (GPP) time series. GPP, the primary photosynthetic carbon flux, underpins ecosystem functioning and is a widely accepted proxy for productivity (Anav et al., 2015; Smith and Boers, 2023a). AR(1), with variance as an auxiliary component, is applied for comparative analysis (Seddon et al., 2016; Smith et al., 2022; Smith and Boers, 2023b, 2023a). Prolonged degradation results in abrupt forest declines (ADs), triggering critical transitions due to reduced resilience (Forzieri et al., 2022; Kéfi et al., 2013; Scheffer et al., 2009). EPR signals were validated through comparison with ADs—identified as GPP anomalies (Hu et al., 2018)—and with event records, including flux-tower observations. Second, given the limited post-disturbance recovery of ecosystems (Arani et al., 2021; Johnson et al., 2025), we identify EPR states across ADs (Gao et al., 2016; Keith et al., 2023). Process characteristics are represented by EPR change amplitude and rate (Arani et al., 2021; Bathiany et al., 2024). Structure attributes—resistance, latitude, and precariousness—reflect recovery capacity limits, systemic change resistance, and proximity to critical thresholds (Folke et al., 2004; Gladstone-Gallagher et al., 2019; Oliver et al., 2015; Walker et al., 2004). These are characterized using basin topologies in terms of basin width, depth (Meyer et al., 2018), and number of alternative attractors (Lohmann et al., 2024). Conceptual quantification and integration enable spatial assessment of EPR dynamics, broadening its applicability to large-scale, real-world ecosystems.

We apply the indicator framework across China, a major contributor to global forest expansion and a key terrestrial carbon sink, where ecological threshold risks are of increasing concern (Guo et al., 2023). China spans multiple climatic zones and exhibits pronounced gradients in elevation and water availability, with distinct temperate–subtropical ecotones (Niu et al., 2025). Long-standing forestry policies further underscore the practical urgency of resilience assessment. Moreover, while climate projections suggest growing hydroclimatic divergence and extremes (Liu et al., 2024; Zaitchik et al., 2023), it remains uncertain whether higher temperatures and CO_2 under high-emission scenarios enhance resilience (Merganičová et al., 2019). Leveraging ensemble GPP datasets (2000–2018), we assess forest EPR dynamics from historical to future climates (2060–2080). Objectives are to: (1) quantify EPR spatiotemporal variation and drivers; (2) validate applicability of CSD metrics for EPR estimation; (3) characterize EPR states and identify potential transitions; (4) assess future risk of EPR across scenarios. By linking carbon sink variability with functional resilience, the framework elucidates mechanisms driving EPR trajectories. It enables pixel-level diagnosis of resilience states, supporting risk mapping, early warning, and adaptive forest management under climate change.

2. Material and methods

We propose a four-module indicator framework integrating satellite-based indices with machine learning (Fig. 1): (1) EPR quantification based on GPP-derived CSD metrics and attribution analysis via boosted regression tree (BRT) models; (2) validation of EPR signal through spatiotemporal alignment of AD events and observed records; (3) identification of EPR states and potential transitions through structure–process characteristics; and (4) assessment of future EPR and transition risks across climate scenarios. The detailed workflow and parameterization are provided in Fig. S2.

2.1. Forest study area selection

To define ecologically representative and consistent forest grid cells, we used three annual land cover datasets: MODIS MCD12Q1(500 m, 2001–2018), ESA-CCI (300 m, 2000–2018), and China Land Cover Dataset (CLCD, 30 m, 2000–2018) (Yang and Huang, 2021) (Table S1). These datasets were chosen for harmonized classification schemes and validated regional accuracy. All data were resampled to 500 m and aggregated into 0.05° × 0.05° grids. Only grid cells with forest cover exceeding 50 % were retained as valid samples. No temporal lag was applied in sample integration, as vegetation responds to climatic fluctuations within one year or less (Gampe et al., 2021; Seddon et al., 2016). Annual data from each product were consolidated, and overlapping samples across datasets were identified. A total of 69,335 cells (0.05° × 0.05°) were retained to define the study area and applied as a spatial mask for analyses. Intact forest accounted for 4.02 % of the study area. Forest types were derived from the Vegetation Map of the People's Republic of China (1: 1,000,000) (Fig. S3), including grass forests, shrub forests, marsh forests, cultivated forests, coniferous forests, coniferous–broadleaf forests, broadleaf forests, and alpine forests.

2.2. Datasets

2.2.1. Gross primary production (GPP) ensemble datasets

To mitigate biases in productivity estimation, we integrated five GPP datasets derived from different modeling approaches, including statistical methods, light use efficiency (LUE) models, and machine learning techniques (Table S2). Statistical models establish relationships between site-level carbon flux observations and remote sensing or climate variables, such as terrestrial vegetation's near-infrared reflectance (NIRv) (Badgley et al., 2017). They effectively capture seasonal and interannual dynamics (Wang et al., 2021b). LUE models, including MODIS (MOD17) (Zhao et al., 2005), the revised EC-LUE (Zheng et al., 2020), and the two-leaf LUE (TL-LUE) (Bi et al., 2022), are computationally efficient and incorporate environmental constraints to improve estimation of vegetation responses (Anav et al., 2015). Machine learning algorithms derive predictive functions from observed patterns and exhibit strong adaptability to complex data structures. FluxSat v2.0 integrates FLUXNET eddy covariance data with satellite observations to produce daily GPP estimates, and performs comparably or better than leading products (Joiner and Yoshida, 2020) (Fig. S4). In this study, EPR were independently derived from each GPP dataset to compare spatiotemporal

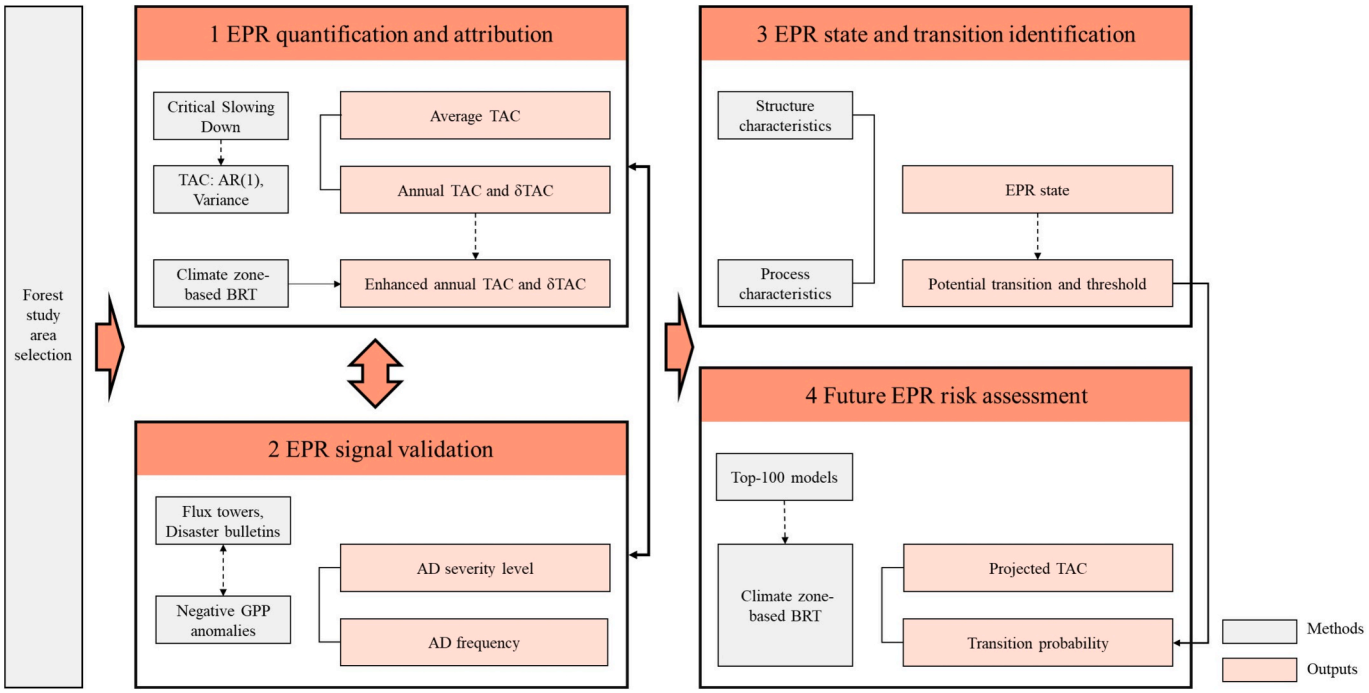

Fig. 1. The indicator framework for assessing forest EPR and transition risk.

consistency. Pixel-level mean EPR values were extracted for subsequent analysis.

2.2.2. Vegetation dynamics data

To monitor vegetation and disturbance responses underlying EPR dynamics, we used three MODIS products: (1) Leaf Area Index (LAI) (MCD15A2H, 500 m, 8–days 2000–2024) (2) Normalized Difference Vegetation Index (NDVI) (MOD13Q1,250 m, 16–days 2000–2024) and (3) Enhanced Vegetation Index (EVI) (MOD13Q1,250 m, 16–days 2000–2024). These datasets were aggregated to 0.05° resolution using spatial averaging.

2.2.3. Climate driver datasets

To assess the influence of climate on EPR, we integrated ground-based observations with downscaled model projections. Monthly data were obtained from the China Meteorological Administration. 427 meteorological stations were selected for data quality, temporal continuity, and spatial representativeness. Variables included maximum and minimum evaporation (EVPmax/EVPmin), precipitation (PRE), air temperature (TEM), air pressure (PRS), relative humidity (RHU), sunshine duration (SSD), wind speed (WIN), and ground surface temperature (GST, 0 cm). Future climate projections were derived from ten General Circulation Models (GCMs) in the Coupled Model Intercomparison Project Phase 6 (CMIP6): ACCESSCM2, BCCCSM2MR, ECEarth3Veg, FIOESM20, GISSE21G, INMCM50, IPSLCM6ALR, MPIESM12HR, MRIESM20, and UKESM10LL (Table S3). Three shared socioeconomic pathways (SSPs) representing different CO_2 emissions trajectories were selected: low (SSP2–RCP4.5), medium–high (SSP3–RCP7.0), and high (SSP5–RCP8.5). Climate zones, defined by the Committee for Natural Regionalization of the Chinese Academy of Sciences, were classified into temperate, central subtropical, and plateau types based on forest distribution (Fig. S3).

2.2.4. Standardized precipitation evapotranspiration index (SPEI)

SPEI, calculated from precipitation and potential evapotranspiration using the Penman–Monteith method, is a widely adopted index of climate variability (Gampe et al., 2021; Guo et al., 2023; Jiao et al., 2021). The 3-month SPEI series from the same meteorological stations was used to identify soil moisture and vegetation water availability (Wang et al., 2021a). SPEI values were categorized into water deficit (SPEI ≤ -0.5), normal state ($-0.5 <$ SPEI < 0.5), and water surplus (SPEI ≥ 0.5), with greater absolute values indicating larger anomalies. Geographically Weighted Regression Kriging (GWRK) was used to interpolate continuous SPEI surfaces from station observations. This method first applied GWR to model spatial relationships between SPEI and environmental covariates, producing a local trend surface. Residuals were interpolated via ordinary kriging with a fitted semivariogram and combined with the trend to produce the final surface (Bahmani et al., 2021). The dataset was randomly divided into 342 calibration and 85 validation sites. Residual normality was assessed using the one-sample Kolmogorov–Smirnov test, and predictive performance was evaluated through 10-fold cross-validation (CV) (Table S4).

2.3. EPR indicator framework

2.3.1. Deseasoning and detrending

To ensure stationarity and avoid spurious alarms, seasonal-trend decomposition by Loess (STL) was applied to each pixel (Cleveland et al., 1990). Seasonality and long-term trends were removed from all GPP and vegetation datasets (LAI, EVI, NDVI), and only the residual component was retained for EPR estimation. Climatic and vegetation predictors were retained with original variability to ensure robust attribution analysis.

2.3.2. EPR quantification and attribution analysis

EPR was quantified using AR(1), with variance used to assess the consistency of temporal trends (Forzieri et al., 2022; Scheffer et al., 2009; Smith et al., 2022). This indicator, calculated over the entire time series for forest pixels, is referred to as the average TAC.

To explore drivers of EPR, Boosted Regression Tree (BRT) models were employed across climate zones. BRT is a machine learning method that combines boosting and regression, optimizing learning rate and tree complexity to improve performance (Elith et al., 2008; Friedman, 2001). It effectively handles missing data and nonlinear interactions (Hong et al., 2020). The model used average TAC as the response variable. Predictors included vegetation (forest cover and NDVI) and climate

variables (EVP, PRE, TEM, PRS, RHU, SSD, WIN, and GTS) (Bochow and Boers, 2023; Forzieri et al., 2022; Liu et al., 2024; McDowell et al., 2020) (Table S5). All predictors were standardized using z-scores (Friedman, 2001), and models were implemented using the 'gbm' R package. To mitigate overfitting, 80 % of the data was used for training and 20 % for validation. Model tuning and performance evaluation were conducted using 10-fold CV. The optimal parameters included a tree complexity of 5, a bag fraction of 0.5, and a learning rate of 0.005 or 0.01 depending on the sample size. For each climate zone, 100 BRT models were constructed, and the median prediction was used as the final EPR estimate (Fig. S5).

Annual TAC time series and their temporal trends were analyzed using a 3-year sliding window, which balances sensitivity to abrupt shifts and statistical robustness over the study period (Forzieri et al., 2022; Smith et al., 2022). Climate zone-based BRT models were applied to disentangle climatic and vegetation contributions, removing confounding signals from the vegetation-driven TAC. Long-term linear trends in the enhanced TAC series (δTAC) were used as the CSD indicator. δTAC was calculated using Kendall rank correlation (τ) applied to AR(1) and variance time series. A τ value of 1 or − 1 indicates a persistent increasing or decreasing trend, respectively. Statistical significance was tested using 10,000 phase-shuffled surrogates, generated by Fourier transform with randomized phases and inverse reconstruction to preserve variance and autocorrelation (Dakos et al., 2008; Smith et al., 2022). A threshold of $P < 0.05$ was used.

Site-level validation was conducted at four flux tower sites—Xishuangbanna, Dinghushan, Qianyanzhou, and Changbaishan—spanning tropical to temperate forests with distinct hydroclimatic conditions (Fig. S3). At each site, CSD indicators of forest pixels were compared with monthly variability in GPP derived from 2003 to 2010 flux observations.

2.3.3. Characterizing of EPR states and transition

To characterize EPR states under varying levels of ecosystem degradation, we identified forest ADs. ADs were defined as negative GPP anomalies during the growing season (May–October), relative to the long-term mean. For each pixel i, month m, and year y, the baseline monthly mean $\mu_{i,m}$ and standard deviation $\sigma_{i,m}$ were calculated from 2000 to 2018 GPP data. An AD of severity level $n \in \{1, 2, \cdots, 6\}$ was recorded when:

$$GPP_{i,m,y} < \mu_{i,m} - n \times \sigma_{i,m} \quad (1)$$

where n is the largest value for which Eq. (1) holds. An AD was retained only if the anomaly was concurrently detected in at least two satellite products. Larger n values reflect more extreme deviations and severe ecosystem alterations. We employed the Mann–Whitney U test to examine statistical relationships between identified ADs and preceding TAC values, assessing whether more severe events were associated with higher antecedent TAC.

To assess general EPR responses to climate variability across ADs, we binned the data using percentile thresholds (1st–99th). Using the binned averages, 100 bootstrap nonlinear regressions were conducted to quantify the amplitude and rate of EPR change to climate variability, representing process characteristics. Kernel density estimation was applied to quantify TAC distribution and detect potential multimodality. Gaussian Mixture Models were fitted to the density curves, with the number of components determined by CV and the Bayesian Information Criterion. Attractor width, depth, and number were extracted from the fitted parameters to characterize the EPR structure attributes. These structure–process characteristics across ADs facilitated the identification of distinct states and transitions.

2.3.4. Assessment of EPR transition under future climate change

To project EPR and occurrence probabilities of transitions, we established climate zone-based BRT models (Fig. S6). The models were driven by monthly temperature and precipitation from GCMs, averaged over future time windows. An ensemble of 100 top-performing random models was used to generate the final spatial predictions. To categorize regions as at-risk or not at-risk based on successive transition occurrence probabilities, a threshold was determined by maximizing sensitivity and specificity using the 2016 data (excluding the last two years due to AR (1) instability from the moving window). The final cutoff was derived as the mean optimal value across folds (Fig. S7) and was applied to classify future risk under each RCP.

2.3.5. Uncertainty and robustness analysis

We tested the robustness of EPR estimates by adjusting sensitive processing parameters. As vegetation indices are widely used to assess ecosystem resilience (Oliver et al., 2015; Smith and Boers, 2023b), we compared δTAC derived from vegetation indices (NDVI, EVI, and LAI) and GPP to evaluate consistency (Fig. S8). Uncertainties were further assessed by applying a stricter seasonal decomposition setting (seasonal = 13) instead of "periodic", and by varying the sliding window length (5-year) in AR(1), variance, and Kendall τ calculations (Figs. S9 and S10).

3. Results

3.1. Forest EPR decline is primarily driven by climatic water availability

Vegetation indices (NDVI, EVI, LAI) increased significantly in most regions, except for a decline in the southeastern plateau zone (Fig. S11). Climatic water deficits were most pronounced at the boundary between temperate and central subtropical regions, whereas an increase in water surplus occurred across central subtropical and northeastern temperate areas (Fig. S11d). The study area exhibited a high average GPP (121.55 $gCm^{-2}month^{-1}$) with a significant upward trend, except in some plateaus and northwestern temperate regions (Fig. S4). TAC values were generally higher in plateau and central subtropical areas but lower in temperate and southernmost regions (Fig. 2a; Fig. S12). The lowest average EPR was observed along the boundary between the plateau and central subtropical zones. The central subtropical zone also showed the most pronounced decreasing trend. Variance trends were generally consistent with the latitudinal pattern of δTAC, exhibiting a significant upward EPR trend at northernmost latitudes (Fig. 2b; Fig. S13). Notably, 55.64 % of forests showed declining EPR as well as increasing GPP trends (δGPP) (Fig. 2c). This pattern was most evident in the central subtropical zone, resulting in expanding yet more vulnerable carbon sinks.

The BRT revealed that the average TAC was primarily driven by NDVI, EVPmin, and SPEI, with pronounced nonlinear interactions (Fig. 2d). Attribution analysis showed that climate variability accounted for over 90 % of the variation in annual TAC and δTAC. Tmax, SPEI, and PRE—variables linked to climatic water availability—emerged as the dominant drivers (Fig. 2e). In temperate forests, SPEI was identified as the strongest predictor, with both water deficit and surplus diminishing EPR (Fig. S14).

3.2. Statistical link between EPR signal and abrupt decline under water surplus and deficit

Throughout the study period, forest ADs exhibited higher frequency and severity at northern latitudes and diminished towards the south (Figs. 3a and b). Coniferous-broadleaf and broadleaf forests in the northern temperate zone experienced the highest total AD frequencies (49.40 events). Central subtropical shrub forests had the lowest AD frequency (17.43 events) and severity (n = 1–2). For forest pixels, TAC in the month antecedent to an AD event was consistently higher than in months without AD and increased with AD severity. These patterns were statistically significant across all datasets ($P < 0.001$).

Remote sensing–derived TAC signals showed spatiotemporal

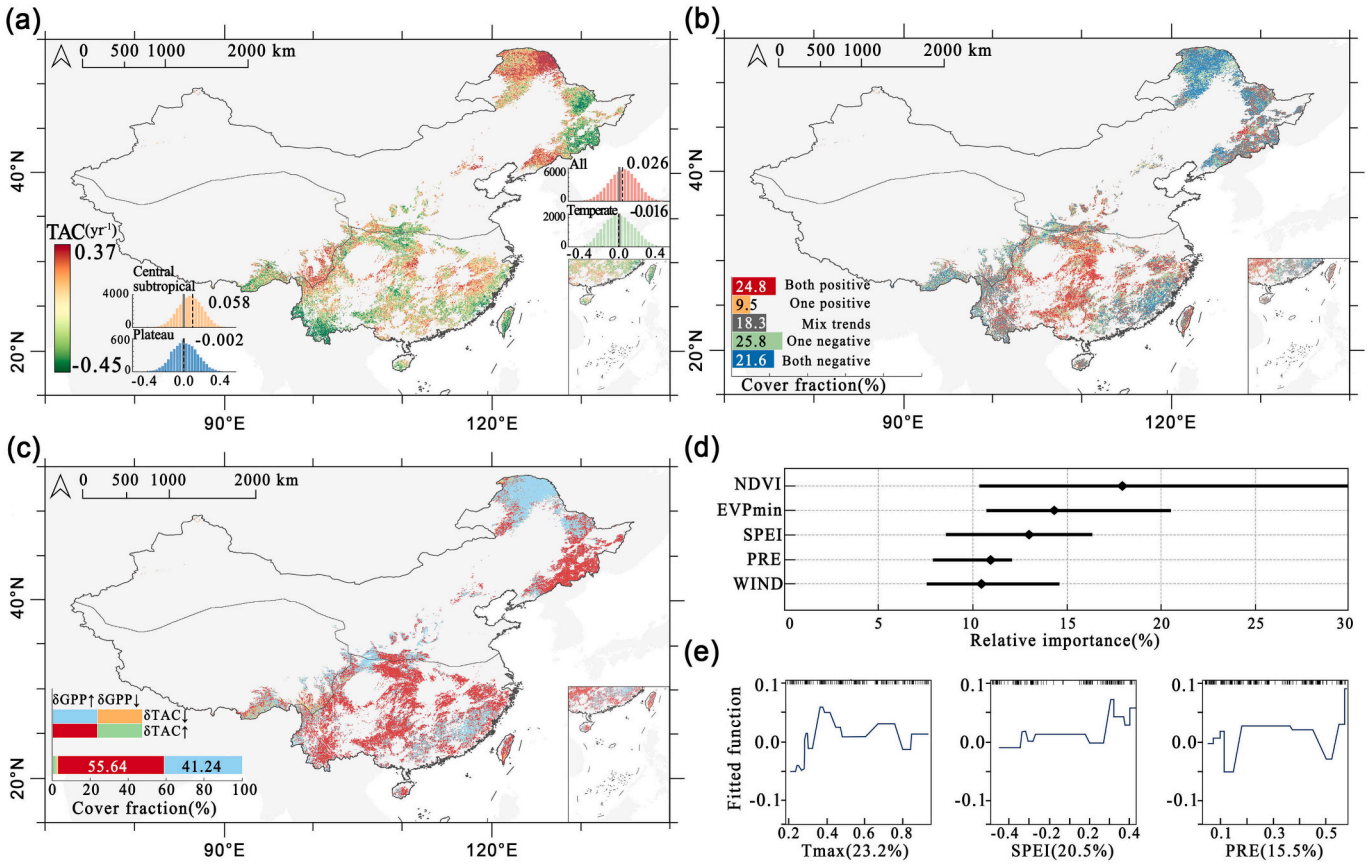

Fig. 2. Spatiotemporal variation of forest EPR and its drivers. (a) Spatial distribution of average TAC, with each pixel representing the mean across datasets during the study period. Frequency distribution of TAC trends (δTAC) categorized by climate zones, with vertical dashed lines showing the distribution mean. (b) Direction of EPR trends (positive/negative) for annual AR(1) and variance. Linear trends are calculated based on 3-year rolling window estimates; only trends with $P < 0.05$ are shown in colors. (c) Spatial distribution of areas with four combinations of GPP trends (δGPP) and δTAC decreases/increases indicated by different colors. (d) Dominant driving factors of average TAC, with each factor's contribution range derived from all datasets. (e) Dominant factors and partial dependence relationships driving δTAC, with solid lines indicating median responses across 100 model runs.

alignment with observed events. Sharp TAC increases coincided with high-frequency GPP anomalies during the growing season and with documented severe droughts and flooding (Figs. 3c and d). Variance trends were similar to TAC but less sensitive in capturing anomalies (Fig. S15). At the site scale, changes in TAC were significantly correlated with intermonthly GPP variability across flux tower sites ($P < 0.05$; Fig. S16). Consistent temporal patterns were also observed across vegetation types, with δTAC values indicating a general EPR decline (Fig. S17). Type-specific differences in EPR magnitude and variability were aligned with observed ADs ($P < 0.001$).

Climatic water availability, represented by SPEI, showed significant differences between forest pixels experiencing ADs and those without ($P < 0.001$). Specifically, water deficit and surplus were associated with AD occurrence in 98.62 and 95.62 % of the area, respectively (Figs. 4a and b). In the central subtropical zone, central regions were widely affected by water deficit, while eastern areas suffered extensively from water surplus. The temperate zone, with a broad SPEI range and frequent anomalies, was highly vulnerable to both water surplus and deficit (Fig. 4c). Most vegetation types were more sensitive to water deficit; however, coniferous-broadleaf forests, alpine forests, and marsh forests were particularly prone to severe ADs in water surplus conditions (Fig. 4d). Additionally, a few severe AD events ($n = 6$) occurred under normal SPEI without detectable climatic anomalies (Fig. S18) and were excluded from subsequent analyses.

3.3. EPR states transition from uniform stability to unstable multistability

Relationships between EPR and climatic water availability exhibited regionally nonlinear patterns, and EPR state characteristics varied across ADs. In the central subtropical zone, forests showed weaker resistance to water deficit compared to surplus (average change rate: 0.82 (0.72); Fig. 5a). With increasing water surplus, forests in the plateau climate zone displayed the lowest recovery rate (average change rate: 1.21(0.24, 0.72)). When water became scarce, TAC in temperate forests exhibited concentrated anomalies, leading to a sudden EPR decline. Increasing AD severity further heightened the sensitivity of EPR responses (Fig. 5b), with fluctuations around the median of bins becoming progressively larger ($P < 0.001$). Under climatic positive feedback, forests experiencing more severe ADs showed an accelerated decline in recovery rate ($P < 0.001$).

Notably, two distinct EPR states were identified based on structure–process characteristics. The EPR of forests experiencing small ADs ($n = 1$–3) exhibited more concentration and less variation, showing a gradual, threshold-dependent but reversible pattern. The TAC response to SPEI exhibited a unimodal distribution ($P < 0.05$) with a single wide and deep attractor ($P < 0.001$), representing the uniform stability (State I) (Fig. 5c). Conversely, the EPR of forests experiencing severe ADs ($n = 4, 5$) underwent significant step changes, oscillated across regions of phase space, and transitioned among attraction basins. The TAC response to SPEI was multimodal ($P < 0.05$), with two close-by but disconnected narrow and shallow attractors ($P < 0.001$), defining the unstable multistability (State II) (Fig. 5d). This marks the critical

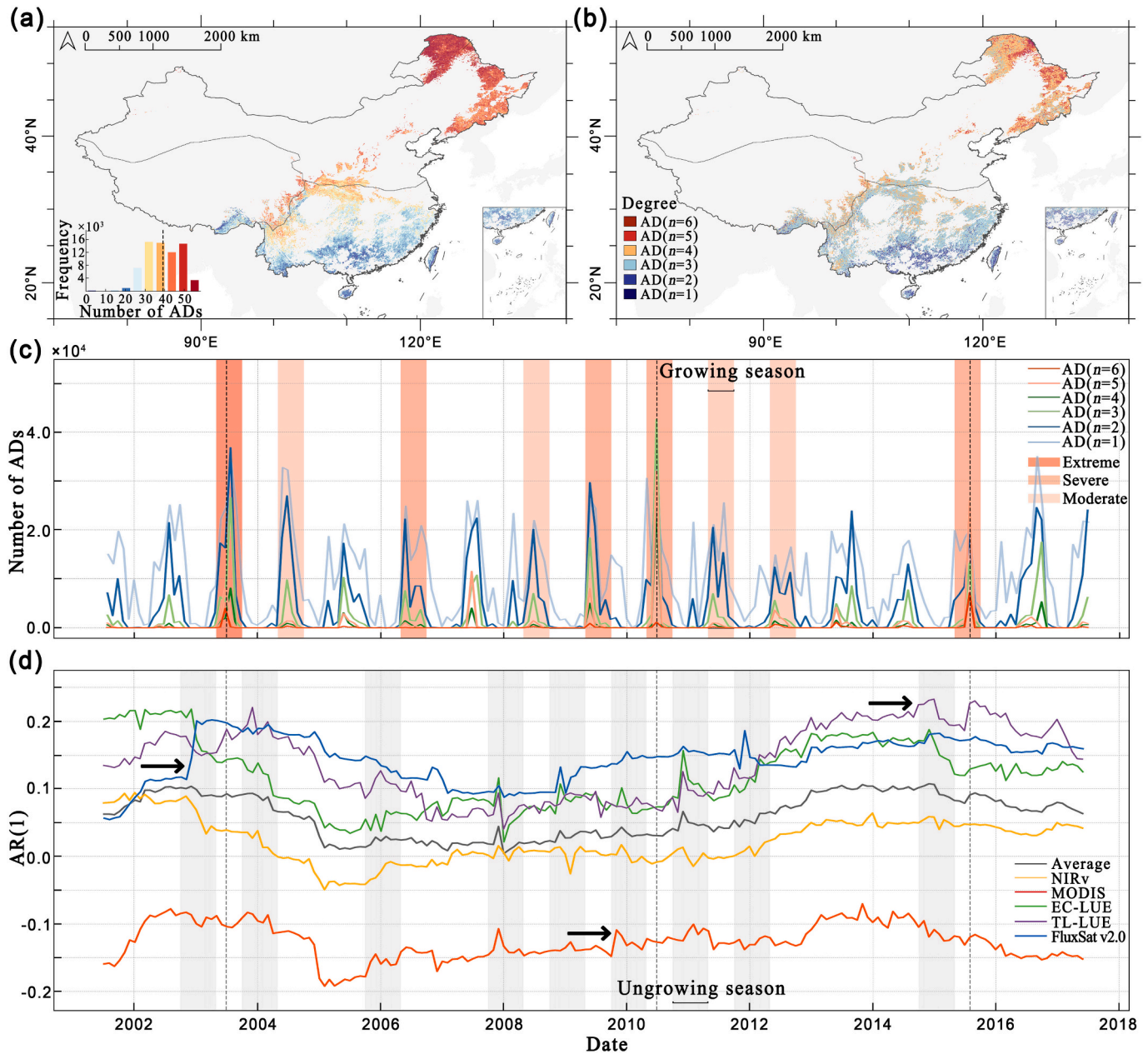

Fig. 3. Abrupt forest declines (ADs) spatial distribution and EPR signals. (a) Spatial distribution of total AD frequency during the study period. (b) Spatial distribution of ADs in the most severe level. (c) Trends in total monthly AD frequency at different levels (n = 1–6), with higher weights assigned to severe declines due to greater destructiveness for visualization. (d) Monthly average AR(1) time series. Red bands during the growing season indicate hydroclimatic damage levels reported in the China Flood and Drought Disaster Bulletin. Severe years (July 2003, June 2010, July 2015) coincided with peaks in GPP anomalies. Black arrows mark AR(1) peaks occurring in or near these years, and black dashed lines indicate the timing of shift occurrences in GPP datasets. AR(1) captures varying levels of ADs earlier in grey bands. These peak values might manifest earlier in the TAC time series than ADs owing to their calculation within a moving window.

transition in EPR from uniform stability (State I) to unstable multi-stability (State II). State II is characterized by a complex landscape of coexisting narrow and shallow attraction basins, as well as high amplitudes and rates of CSD change. Overall, 24.58 % of forests underwent this critical transition (AD (n = 4): 21.19 %, AD (n = 5): 3.39 %), with the highest occurrence rates observed in coniferous-broadleaf (37.32 %) and broadleaf forests (30.95 %). Given the dual impacts of water surplus and deficit, the thresholds most likely to occur under both conditions were recorded as the maximum limits a balanced ecosystem could tolerate. Remarkably, most transitioned forests occurred in boundary regions at the convergence of diverse climates, topographies, tectonic environments, and biomes (Figs. 5e and f).

3.4. Escalating spatial risk of forest EPR under future climate scenarios

Our results revealed a spatially persistent and intensifying pattern of EPR risk from historical to future climate across scenarios. Importantly, SSP2-4.5 is projected as the worst-case EPR scenario for 2060–2080, with climate variables leading to the highest transition occurrence probabilities (0.18; (95 % CI:0.05–0.89)) and most significant EPR loss (Fig. 6). Applying a probability threshold of 0.11(Fig. S7), up to 67.15 % of China's forests would be at risk of EPR critical transition (Fig. 6a). High probabilities occurred mainly in plateau and southern temperate forests, particularly in boundary areas. These regions coincide with areas projected to experience significant increases in temperature and precipitation (Fig. S19). Furthermore, under SSP2-4.5 scenario, 59.22 %

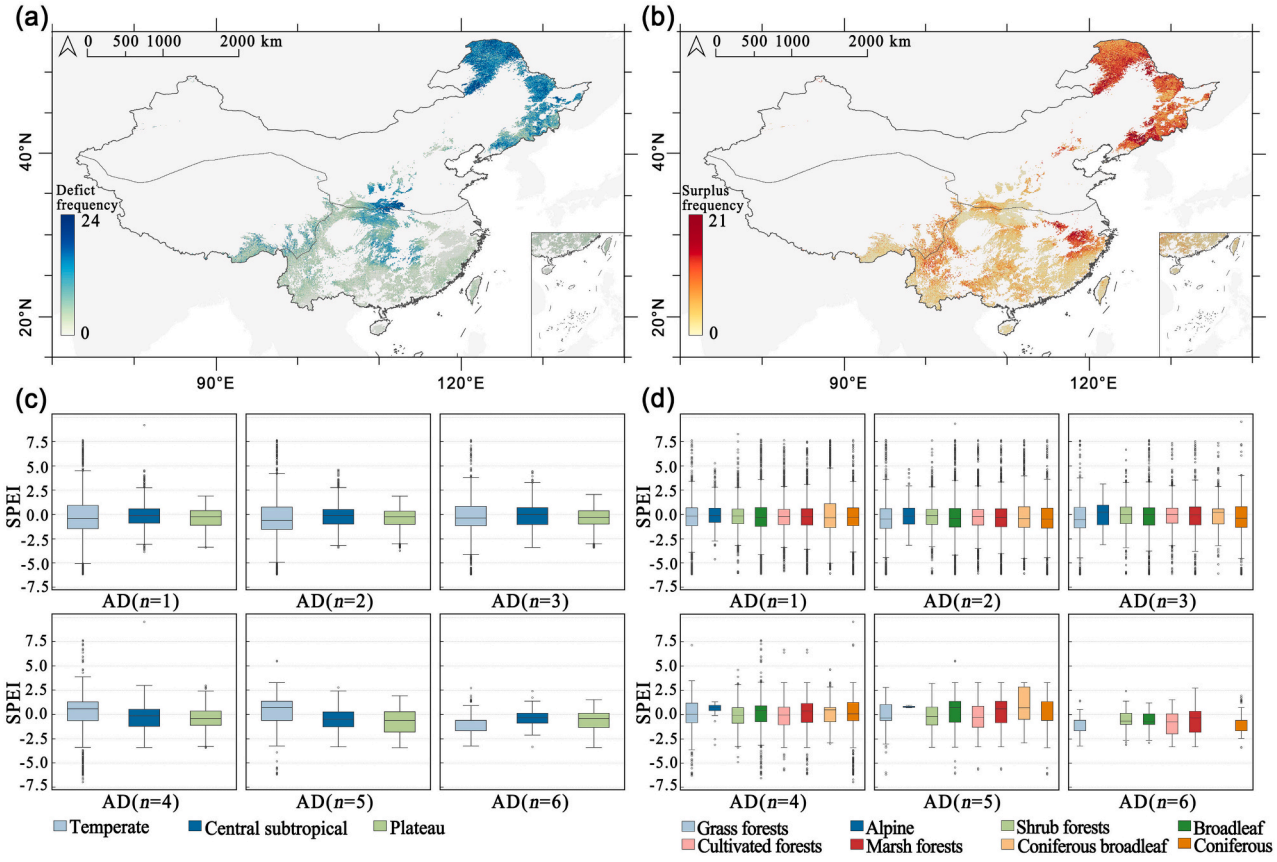

Fig. 4. Response relationships between abrupt forest declines (ADs) and climatic water availability. Spatial distribution of AD frequency under water deficit (a) and water surplus (b) during the study period. Range of SPEI values for forest AD occurrence across different climate zones (c) and vegetation zones (d). Box plots showing 1000 randomly sampled surrogates across zones. The edges of the boxes represent the 25th and 75th percentiles, with black lines indicating the median. Whiskers illustrate the data range, and outliers are shown as dots.

of forests are expected to continuously decline in EPR, with the most pronounced deterioration in plateau and central subtropical zones (Fig. 6b). In eastern subtropical zones, increasing risks are mainly driven by substantially increased precipitation (53.8 %) rather than reduced temperature (46.2 %) (Fig. S6b). This pattern exacerbates the negative impacts of water surplus (Fig. 4b). In contrast, under the SSP5-8.5 scenario, temperate forests are expected to undergo the greatest average EPR improvement. Temperate forests benefit more from rising temperatures, with the relative importance of 59.3 % (Fig. S6a), alleviating water surplus limitations. Notably, up to 96.32 % of forests predicted to experience declining EPR are currently undergoing positive GPP trends, accounting for 57.04 % of the study area (Fig. 6c). Although the proportion of vulnerable carbon sinks has slightly increased compared with recent decades (Fig. 2c), their distribution has shifted markedly toward the productive south.

4. Discussion

4.1. Application of critical slowing down in ecosystem function

Critical slowing down has emerged as an effective approach for measuring ecosystem resilience and anticipating critical transitions (Dakos et al., 2015; Liu et al., 2023; Scheffer et al., 2009). Its application across China's forests confirmed its robustness in EPR estimation, a key dimension of functional resilience. This finding is supported by consistent spatiotemporal patterns (Fig. 1; Figs. S9 and S10) and by alignment with previous studies (Forzieri et al., 2022; Piao et al., 2005; Seddon et al., 2016; Smith et al., 2022). TAC analysis provided early signals of ecosystem degradation severity, as evidenced by correspondence with ADs and record events (Fig. 3), extending the resilience theoretical framework.

The indicator system facilitates fine-scale assessment of EPR variation, revealing previously overlooked patterns. Central subtropical forests, crucial carbon sinks with notable growth (Aguirre-Gutiérrez et al., 2022; Smith and Boers, 2023a), are experiencing a persistent EPR decline projected to continue. Conversely, despite productivity declines amid frequent anomalies (Forzieri et al., 2022), northern forests are projected to experience increasing EPR (Fig. 2a–c). It should be noted that EPR may not increase consistently with greening or carbon sink growth (Yan et al., 2025), highlighting delayed responses and potential structural–functional decoupling. Coniferous-broadleaf forests exhibited the highest yet most variable EPR, while coniferous forests showed the lowest levels (Fig. S17); both were associated with elevated transition risks (Fig. 5; Smith and Boers, 2023b). Mixed forests benefit from trait diversity, but structural complexity could amplify temporal fluctuations (Lipoma et al., 2024) or induce resilience inertia (Aguirre-Gutiérrez et al., 2025). In contrast, broadleaf forests tend to show low resistance to water variability (Xu et al., 2024). This underscores the need to prioritize long-term resilience over short-term provisioning and to incorporate linkages among structure, processes, and functions into monitoring frameworks. Moreover, climatic water availability emerged as a dominant driver of EPR variation (Fig. 2e; Poorter et al., 2016). While most studies have emphasized the impacts of water deficit (Gampe et al., 2021; Guo et al., 2023; Li et al., 2023; Liu et al., 2024), the anomalies attributed to water surplus merit further investigation (Fig. 4).

In this study, the 3-year window was more effective in capturing abrupt EPR shifts; the 5-year window improved trend stability but

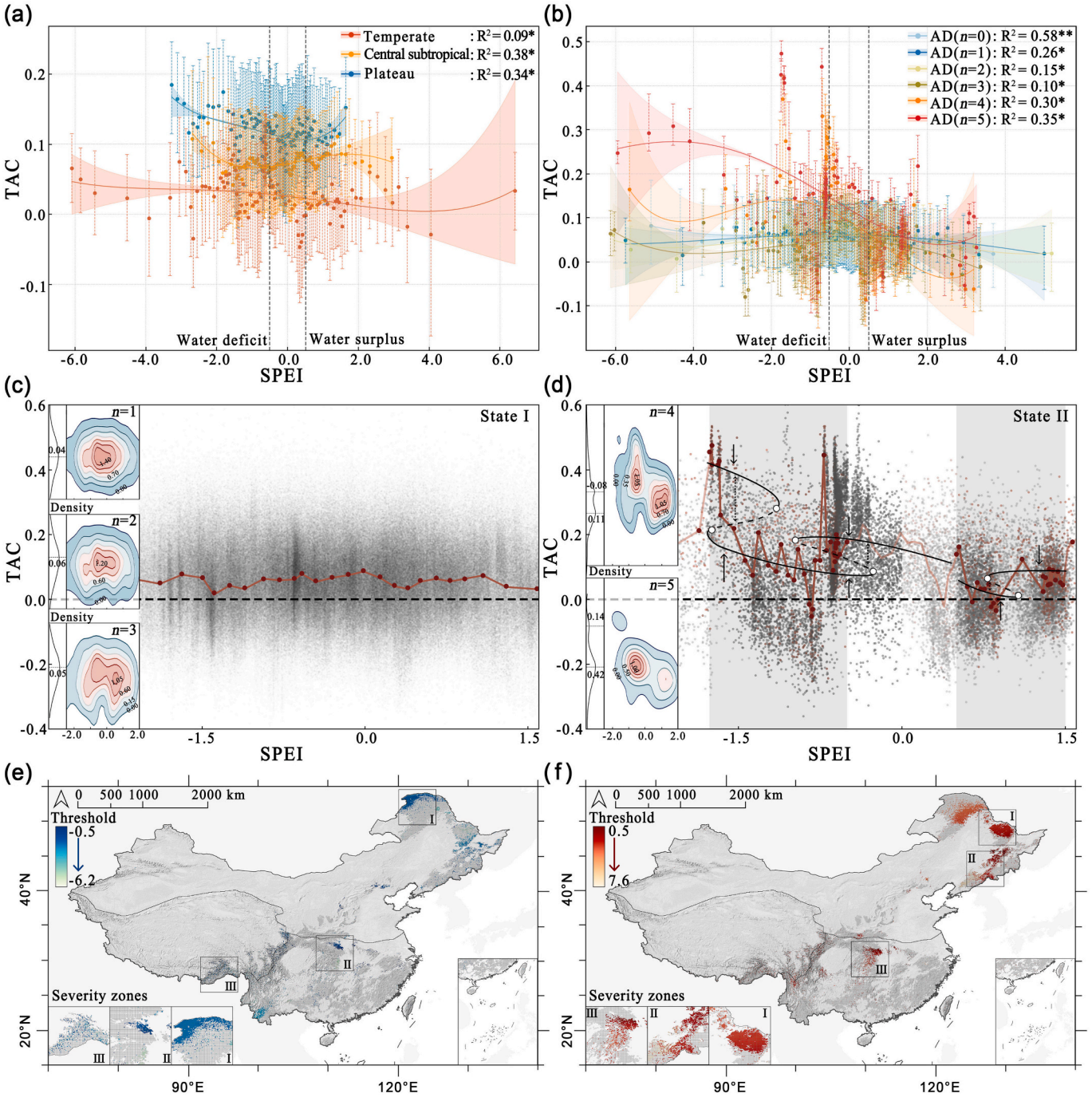

Fig. 5. State transition in forest EPR and critical thresholds under climatic water availability. (a) Relationship between SPEI and EPR in forests experiencing ADs, categorized by climate zones. (b) Relationship between SPEI and EPR in forests experiencing ADs, categorized by the severity of ADs. For comparison, the response of ecosystems without ADs ($n = 0$) was also included. For ADs ($n = 4$, 5) analysis, bins with fewer than 100/10 members and other analysis bins with fewer than 1000 members were excluded. Solid dots represent binned medians, with vertical lines and hatches showing 25th–75th percentiles in each bin. Medians were fitted using 100 bootstrapping nonlinear polynomial regressions. The solid line represents the median trend, fitted using bootstrapped regressions, and the colored bar depicts the 95 % confidence interval (CI). * $P < 0.001$; ** $P < 0.05$ (two-sided bootstrap test). Statistical characteristics of the transition from uniform stability (c) to unstable multistability (d). Red lines connecting the bins' median points indicate the maximum fluctuations across ADs. The probability and kernel density distribution on the left of the panel show the variation in width, depth, and attractor number between the two states. The critical transition potential analysis for State II is shown. Solid black lines represent two possible equilibriums, while dashed lines suggest the possible existence of two alternative phases. Small black arrows indicate the direction toward equilibriums. Spatial distribution of critical threshold corresponding to water deficit (e) and water surplus (f) responses. For water surplus, larger thresholds corresponded to greater EPR, whereas for water deficit, smaller thresholds corresponded to greater EPR.

tended to smooth out sudden changes, potentially underestimating early warning signals (Figs. S9–S10 and S15). Among datasets, MODIS and FluxSat v2.0 GPP were found to be more accurate in measuring the EPR trend, though MODIS somewhat overestimated (Fig. 3).

4.2. Characterizing EPR states and potential transitions

This study developed an operational indicator framework to identify EPR states by integrating structure (basin width, center, and attractor

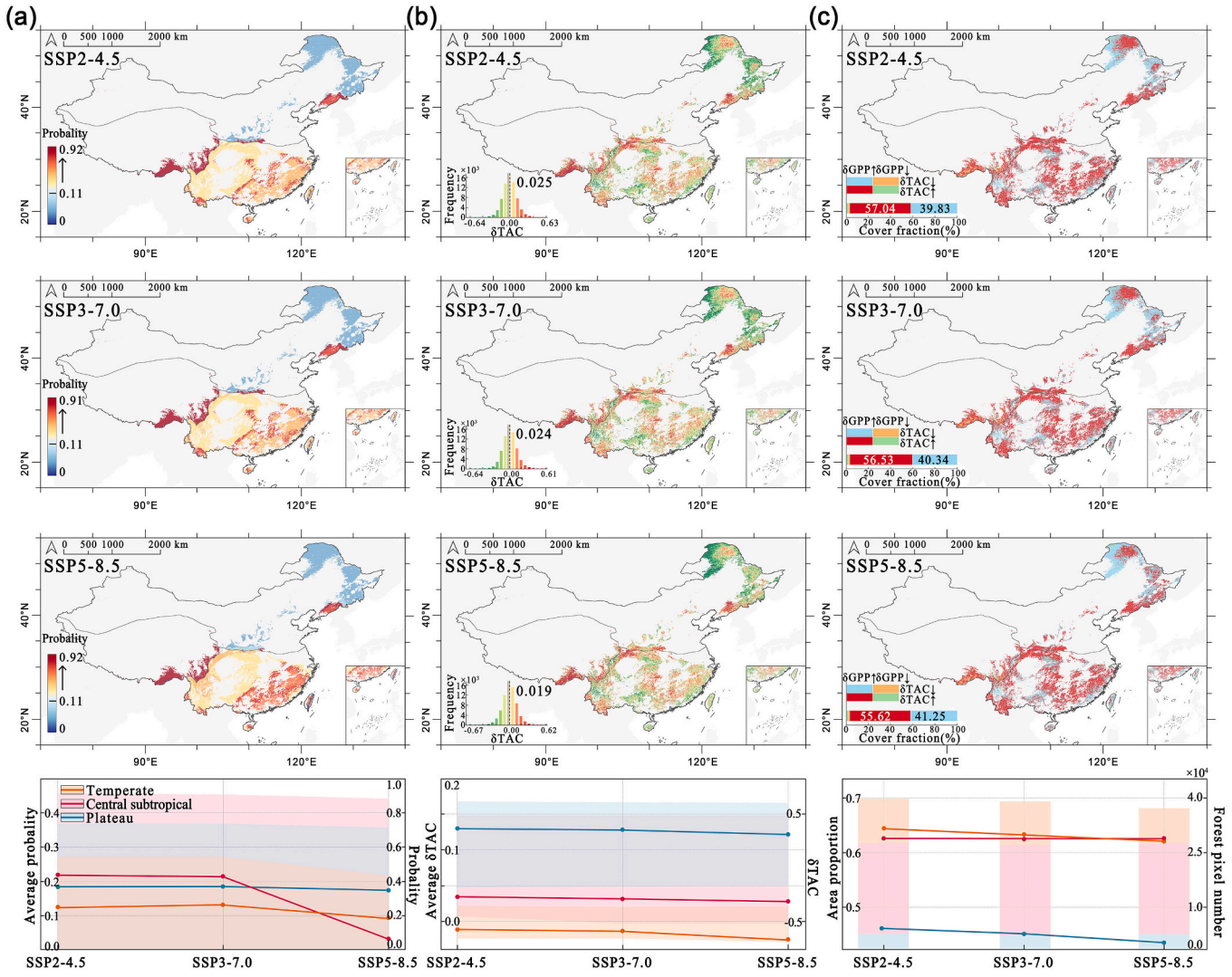

Fig. 6. Assessment of critical transition occurrence probabilities and EPR variation under future climate change. (a) Spatial distribution and variation of transition occurrence probabilities for SSP2-4.5, SSP3-7.0, and SSP5-8.5 in 2060–2080. The bottom panel illustrates the probability variation across climate zones for each scenario, with the solid line representing the average and the colored area indicating the 95% CI change trend. (b) Spatial distribution and variation in forest EPR (δTAC) for SSP2-4.5, SSP3-7.0, and SSP5-8.5 in 2060–2080. Vertical dashed lines in the bar chart represent the distribution average, with the corresponding value shown. The bottom panel illustrates δTAC variations, with the solid line representing the average and the colored area indicating the 95% CI change trend. (c) Spatial distribution and variations of areas with four combinations of decrease/increase GPP trends (δGPP) in 2000–2018 and δTAC in 2060–2080 (indicated by different colors). The bottom panel shows changes in vulnerable carbon sinks (with increasing δGPP and δTAC). The solid line indicates changes in the area proportion of vulnerable carbon sinks under different scenarios within each climate zone, and the stacked chart displays the forest pixel number and proportion of vulnerable carbon sinks.

number) and process (amplitude and rate of change) characteristics. We detected two EPR states across forest ADs, allowing an understanding of complex adaptive ecosystems. The EPR transition from uniform stability to unstable multistability is characterized by coexisting alternative attractors with narrower and shallower basins, as well as higher amplitudes and rates of CSD change (Fig. 5). The dynamic equilibrium of carbon cycling within severe forest ADs has shifted, significantly diminishing capacity for self-organization and adaptive feedbacks under persistent climate change.

For example, certain northern forests under prolonged mild water deficits (SPEI = -1.5 to 0.5) underwent a series of alterations in ecological processes and physiological responses. These likely reflect gradual yet substantial shifts in species composition, favoring drought-tolerant species with lower carbon assimilation capacity (Li et al., 2020). Water stress caused incremental hydraulic failures, constraining transpiration and photosynthesis (Sanchez-Martinez et al., 2025). The ongoing decline in EPR was accompanied by disruptions in carbon and water cycling among vegetation, soil, and the atmosphere, undermining the ecosystem's self-regulatory capacity and stability (Green et al., 2019; Liu et al., 2024). Consequently, long-standing feedback between EPR and environmental conditions has shifted, driving forests into an undesired alternative state. In State II, the complex landscape heightens functional sensitivity to initial conditions and forcing variations. This leads to a sudden decline in ecosystem service capacity and may cross thresholds. Given the dual impact of water availability and uncertainty in tipping dynamics, exact thresholds are not provided for regions where transitions have not yet occurred. We highlight types of climatic disturbances affecting specific regions (Figs. 4a and b) and probabilities of future critical transitions (Fig. 6a).

4.3. *Predicting EPR for adaptive management under rapid climate change*

Our projections suggest the progressive spatial risk of EPR decline and shifts in vulnerability under ongoing climate change. Consistent

patterns reduce uncertainty in future trajectories, enabling effective forest management and planning. The results indicate a sustained positive effect of high-emission scenarios on EPR until the 2060–2080 period, supported by independent studies (Cui et al., 2024; Li et al., 2023). However, edge effects exacerbated by climate variability are likely to have greater negative impacts on biodiversity and ecosystem processes (Gao et al., 2024). Forests located at climatic and geographic boundaries—such as temperate–subtropical ecotones—may therefore be at heightened risk of transition(Fig. 6a). Moreover, management efforts should prioritize mitigating the southward shift of vulnerable carbon sinks, characterized by high productivity, declining resilience, and elevated transition risk. Degradation and fragmentation in low-latitude forests (Aguirre-Gutiérrez et al., 2022; Cook-Patton et al., 2020; Seddon et al., 2016), coupled with heightened sensitivity to climate fluctuations (McDowell et al., 2020; Smith and Boers, 2023a), suggest that antagonistic processes may be occurring.

The proposed framework constructs functional resilience metrics from CSD indicators derived from GPP time series, enabling large-scale EPR assessment in real-world ecosystems. By linking EPR variation with structure–process characteristics, it generates spatially explicit tools for diagnosing risks and anticipating state transitions. The framework serves as a decision-support basis for developing effective mitigation and targeted management in climate-vulnerable regions. In such regions, strategies to counteract water surplus and deficit impacts (Figs. 5a and b) include increasing forest heterogeneity and biodiversity (Flores et al., 2024; Oliver et al., 2015; Poorter et al., 2016), introducing drought-resistant species, and applying water strategies such as withdrawal constraints and efficient irrigation (Li et al., 2023; Merganičová et al., 2019). Resilience-informed interventions are essential for ecological restoration and climate adaptation (Cook-Patton et al., 2020; McDowell et al., 2020; Rietkerk et al., 2021), thereby facilitating ecosystem maintenance or transformation into desirable configurations (Chaparro-Pedraza and de Roos, 2020; Folke et al., 2004; Scheffer et al., 2001).

4.4. Limitations and future perspectives

While our approach leverages remotely sensed GPP datasets and CSD indicators to estimate EPR, several uncertainties remain. These include sensor noise, input data heterogeneity, and inherent limitations of GPP products (Smith et al., 2023; Wang et al., 2021b). Additionally, as SPEI lacks direct representation of soil moisture and streamflow, it may reduce sensitivity to certain hydrological stress signals. At the framework level, exogenous disturbances (e.g., logging, pathogens) and vegetation structure or functional traits are not incorporated, limiting process-based ecological interpretation. Future work should incorporate trait-based resilience mechanisms and capture cross-scale hydroclimatic variability and interactions (Lenton et al., 2024). Combining flux tower and field observations with remote sensing would further strengthen the assessment of resilience and transition risk.

5. Conclusions

This study develops a composite indicator framework to estimate EPR and identify transitions across China's forests. By integrating CSD with resilience characteristics, it enables a large-scale assessment of transition risks. The key findings are as follows: (1) CSD metrics derived from GPP effectively estimate EPR, a key dimension of ecosystem functional resilience, and reveal its degradation, which is statistically linked to abrupt productivity declines; (2) structure–process characteristics of EPR support the identification of state transitions from uniform stability to unstable multistability; (3) predictive patterns of high-risk boundary areas and high-vulnerability spatial shifts provide actionable insights for climate mitigation and adaptation. The framework is applicable to diverse terrestrial ecosystems and ecosystem functioning, providing a science-based and spatially explicit tool for regeneration, restoration, and afforestation. Given the increasing and persistent impacts of climate change on ecosystem tipping dynamics, this study promotes EPR monitoring as an urgent priority for ecological planning and policy development.

CRediT authorship contribution statement

Yingshuo Lyu: Writing – review & editing, Writing – original draft, Visualization, Validation, Software, Methodology, Formal analysis, Data curation, Conceptualization. **Xi Zheng:** Writing – review & editing, Supervision, Funding acquisition, Conceptualization. **Han Wang:** Writing – review & editing, Methodology, Formal analysis. **Teng Liu:** Writing – review & editing, Methodology, Formal analysis. **Chutong Chao:** Writing – original draft, Software, Data curation. **Xiaoyang Ou:** Visualization, Formal analysis.

Declaration of competing interest

The authors declare the following financial interests/personal relationships which may be considered as potential competing interests: Xi Zheng reports financial support was provided by National Natural Science Foundation of China. If there are other authors, they declare that they have no known competing financial interests or personal relationships that could have appeared to influence the work reported in this paper.

Acknowledgments

This work was financially supported by the National Natural Science Foundation of China (Grant No. 32371643).The authors would like to extend their gratitude to the anonymous referees for their constructive feedback, which greatly contributed to improving this manuscript.

Appendix A. Supplementary data

Supplementary data to this article can be found online at https://doi.org/10.1016/j.ecolind.2025.114388.

Data availability

Forest cover datasets are publicly available at https://www.earthdata.nasa.gov/data/catalog/lpcloud-mcd12q1-061; https://www.esa-landcover-cci.org/; https://zenodo.org/records/15853565. Daily SPEI datasets were obtained from https://doi.org/10.6084/m9.figshare.12568280. Downscaled climate projections of CMIP6 are available at https://www.worldclim.org/data/cmip6.html. GPP datasets were obtained from https://doi.org/10.6084/m9.figshare.12981977.v2; https://doi.org/10.5067/MODIS/MOD17A2H.061; https://doi.org/10.6084/m9.figshare.8942336.v3; https://doi.org/10.5061/dryad.dfn2z352k; https://doi.org/10.3334/ORNLDAAC/1835. Vegetation datasets are available at https://doi.org/10.5067/MODIS/MCD15A2H.006; https://doi.org/10.5067/MODIS/MOD13Q1.061. Flux tower observations were derived from https://www.chinaflux.org/index.aspx. All model code is available from the references studies (Liu et al., 2023; Smith and Boers, 2023b).

No new algorithms were developed in this study. Relevant codes for analyzing China's forests are available from the corresponding author upon reasonable request.

References

Aguirre-Gutiérrez, J., Berenguer, E., Oliveras Menor, I., Bauman, D., Corral-Rivas, J.J., Nava-Miranda, M.G., Both, S., Ndong, J.E., Ondo, F.E., Bengone, N.N., Mihinhou, V., Dalling, J.W., Heineman, K., Figueiredo, A., González-M, R., Norden, N., Hurtado-M, A.B., González, D., Salgado-Negret, B., Reis, S.M., Moraes de Seixas, M.M., Farfan-Rios, W., Shenkin, A., Riutta, T., Girardin, C.A.J., Moore, S., Abernethy, K., Asner, G.P., Bentley, L.P., Burslem, D.F.R.P., Cernusak, L.A., Enquist, B.J., Ewers, R.

M., Ferreira, J., Jeffery, K.J., Joly, C.A., Marimon-Junior, B.H., Martin, R.E., Morandi, P.S., Phillips, O.L., Bennett, A.C., Lewis, S.L., Quesada, C.A., Marimon, B. S., Kissling, W.D., Silman, M., Teh, Y.A., White, L.J.T., Salinas, N., Coomes, D.A., Barlow, J., Adu-Bredu, S., Malhi, Y., 2022. Functional susceptibility of tropical forests to climate change. Nat. Ecol. Evol. 6, 878–889. https://doi.org/10.1038/s41559-022-01747-6.

Aguirre-Gutiérrez, J., Díaz, S., Rifai, S.W., Corral-Rivas, J.J., Nava-Miranda, M.G., González-M, R., Hurtado-M, A.B., Revilla, N.S., Vilanova, E., Almeida, E., de Oliveira, E.A., Alvarez-Davila, E., Alves, L.F., de Andrade, A.C.S., Lola da Costa, A.C., Vieira, S.A., Aragão, L., Arets, E., Aymard C., G.A., Baccaro, F., Bakker, Y.V., Baker, T.R., Bánki, O., Baraloto, C., de Camargo, P.B., Berenguer, E., Blanc, L., Bonal, D., Bongers, F., Bordin, K.M., Brienen, R., Brown, F., Prestes, N.C.C.S., Castilho, C.V., Ribeiro, S.C., de Souza, F.C., Comiskey, J.A., Valverde, F.C., Müller, S.C., da Costa Silva, R., do Vale, J.D., de Andrade Kamimura, V., de Oliveira Perdiz, R., del Aguila Pasquel, J., Derroire, G., Di Fiore, A., Disney, M., Farfan-Rios, W., Fauset, S., Feldpausch, T.R., Ramos, R.F., Llampazo, G.F., Martins, V.F., Fortunel, C., Cabrera, K.G., Barroso, J.G., Hérault, B., Herrera, R., Honorio Coronado, E.N., Huamantupa-Chuquimaco, I., Pipoly, J.J., Zanini, K.J., Jiménez, E., Joly, C.A., Kalamandeen, M., Klipel, J., Levesley, A., Oviedo, W.L., Magnusson, W.E., dos Santos, R.M., Marimon, B.S., Marimon-Junior, B.H., de Almeida Reis, S.M., Melo Cruz, O.A., Mendoza, A.M., Morandi, P., Muscarella, R., Nascimento, H., Neill, D.A., Menor, I.O., Palacios, W.A., Palacios-Ramos, S., Pallqui Camacho, N.C., Pardo, G., Pennington, R.T., de Oliveira Pereira, L., Pickavance, G., Picolotto, R.C., Pitman, N.C.A., Prieto, A., Quesada, C., Ramírez-Angulo, H., Réjou-Méchain, M., Correa, Z.R., Reyna Huaymacari, J.M., Rodriguez, C.R., Rivas-Torres, G., Roopsind, A., Rudas, A., Salgado Negret, B., van der Sande, M.T., Santana, F.D., Maës Santos, F.A., Bergamin, R.S., Silman, M.R., Silva, C., Espejo, J.S., Silveira, M., Souza, F.C., Sullivan, M.J.P., Swamy, V., Talbot, J., Terborgh, J.J., van der Meer, P.J., van der Heijden, G., van Ulft, B., Martinez, R. V., Vedovato, L., Vleminckx, J., Vos, V.A., Wortel, V., Zuidema, P.A., Zwerts, J.A., Laurance, S.G.W., Laurance, W.F., Chave, J., Dalling, J.W., Barlow, J., Poorter, L., Enquist, B.J., ter Steege, H., Phillips, O.L., Galbraith, D., Malhi, Y., 2025. Tropical forests in the Americas are changing too slowly to track climate change. Science 387, eadl5414. doi:10.1126/science.adl5414.

Anav, A., Friedlingstein, P., Beer, C., Ciais, P., Harper, A., Jones, C., Murray-Tortarolo, G., Papale, D., Parazoo, N.C., Peylin, P., Piao, S., Sitch, S., Viovy, N., Wiltshire, A., Zhao, M., 2015. Spatiotemporal patterns of terrestrial gross primary production: a review. Rev. Geophys. 53, 785–818. https://doi.org/10.1002/2015RG000483.

Anderegg, W.R.L., Schwalm, C., Biondi, F., Camarero, J.J., Koch, G., Litvak, M., Ogle, K., Shaw, J.D., Shevliakova, E., Williams, A.P., Wolf, A., Ziaco, E., Pacala, S., 2015. Pervasive drought legacies in forest ecosystems and their implications for carbon cycle models. Science 349, 528–532. https://doi.org/10.1126/science.aab1833.

Andersen, T., Carstensen, J., Hernández-García, E., Duarte, C.M., 2009. Ecological thresholds and regime shifts: approaches to identification. Trends Ecol. Evol. 24, 49–57. https://doi.org/10.1016/j.tree.2008.07.014.

Arani, B.M.S., Carpenter, S.R., Lahti, L., van Nes, E.H., Scheffer, M., 2021. Exit time as a measure of ecological resilience. Science 372, eaay4895. https://doi.org/10.1126/science.aay4895.

Badgley, G., Field, C.B., Berry, J.A., 2017. Canopy near-infrared reflectance and terrestrial photosynthesis. Sci. Adv. 3, e1602244. https://doi.org/10.1126/sciadv.1602244.

Bahmani, S., Naganna, S.R., Ghorbani, M.A., Shahabi, M., Asadi, E., Shahid, S., 2021. Geographically Weighted Regression Hybridized with Kriging Model for Delineation of Drought-Prone areas. Environ. Model. Assess. 26, 803–821. https://doi.org/10.1007/s10666-021-09789-z.

Bathiany, S., Bastiaansen, R., Bastos, A., Blaschke, L., Lever, J., Loriani, S., De Keersmaecker, W., Dorigo, W., Milenković, M., Senf, C., Smith, T., Verbesselt, J., Boers, N., 2024. Ecosystem resilience monitoring and early warning using Earth observation data: challenges and outlook. Surv. Geophys. https://doi.org/10.1007/s10712-024-09833-z.

Bi, W., He, W., Zhou, Y., Ju, W., Liu, Y., Liu, Y., Zhang, X., Wei, X., Cheng, N., 2022. A global 0.05° dataset for gross primary production of sunlit and shaded vegetation canopies from 1992 to 2020. Sci. Data 9, 213. https://doi.org/10.1038/s41597-022-01309-2.

Bochow, N., Boers, N., 2023. The south American monsoon approaches a critical transition in response to deforestation. Sci. Adv. 9, eadd9973. https://doi.org/10.1126/sciadv.add9973.

Chaparro-Pedraza, P.C., de Roos, A.M., 2020. Ecological changes with minor effect initiate evolution to delayed regime shifts. Nat. Ecol. Evol. 4, 412–418. https://doi.org/10.1038/s41559-020-1110-0.

Cleveland, R.B., Cleveland, W.S., McRae, J.E., Terpenning, I., 1990. STL: a seasonal-trend decomposition. J. Off. Stat. 6, 3–73.

Cook-Patton, S.C., Leavitt, S.M., Gibbs, D., Harris, N.L., Lister, K., Anderson-Teixeira, K. J., Briggs, R.D., Chazdon, R.L., Crowther, T.W., Ellis, P.W., Griscom, H.P., Herrmann, V., Holl, K.D., Houghton, R.A., Larrosa, C., Lomax, G., Lucas, R., Madsen, P., Malhi, Y., Paquette, A., Parker, J.D., Paul, K., Routh, D., Roxburgh, S., Saatchi, S., van den Hoogen, J., Walker, W.S., Wheeler, C.E., Wood, S.A., Xu, L., Griscom, B.W., 2020. Mapping carbon accumulation potential from global natural forest regrowth. Nature 585, 545–550. https://doi.org/10.1038/s41586-020-2686-x.

Cui, J., Zheng, M., Bian, Z., Pan, N., Tian, H., Zhang, X., Qiu, Z., Xu, J., Gu, B., 2024. Elevated CO2 levels promote both carbon and nitrogen cycling in global forests. Nat. Clim. Chang. 1–7. https://doi.org/10.1038/s41558-024-01973-9.

Cumming, G.S., Peterson, G.D., 2017. Unifying research on social–ecological resilience and collapse. Trends Ecol. Evol. 32, 695–713. https://doi.org/10.1016/j.tree.2017.06.014.

Dakos, V., Carpenter, S.R., van Nes, E.H., Scheffer, M., 2015. Resilience indicators: prospects and limitations for early warnings of regime shifts. Philos. Trans. r. Soc. b: Biol. Sci. 370, 20130263. https://doi.org/10.1098/rstb.2013.0263.

Dakos, V., Scheffer, M., van Nes, E.H., Brovkin, V., Petoukhov, V., Held, H., 2008. Slowing down as an early warning signal for abrupt climate change. PNAS 105, 14308–14312. https://doi.org/10.1073/pnas.0802430105.

Elith, J., Leathwick, J.R., Hastie, T., 2008. A working guide to boosted regression trees. J. Anim. Ecol. 77, 802–813. https://doi.org/10.1111/j.1365-2656.2008.01390.x.

Flores, B.M., Montoya, E., Sakschewski, B., Nascimento, N., Staal, A., Betts, R.A., Levis, C., Lapola, D.M., Esquível-Muelbert, A., Jakovac, C., Nobre, C.A., Oliveira, R. S., Borma, L.S., Nian, D., Boers, N., Hecht, S.B., ter Steege, H., Arieira, J., Lucas, I.L., Berenguer, E., Marengo, J.A., Gatti, L.V., Mattos, C.R.C., Hirota, M., 2024. Critical transitions in the Amazon forest system. Nature 626, 555–564. https://doi.org/10.1038/s41586-023-06970-0.

Folke, C., Carpenter, S., Walker, B., Scheffer, M., Elmqvist, T., Gunderson, L., Holling, C. S., 2004. Regime shifts, resilience, and biodiversity in ecosystem management. Annu. Rev. Ecol. Evol. Syst. 35, 557–581. https://doi.org/10.1146/annurev.ecolsys.35.021103.105711.

Forzieri, G., Dakos, V., McDowell, N.G., Ramdane, A., Cescatti, A., 2022. Emerging signals of declining forest resilience under climate change. Nature 608, 534–539. https://doi.org/10.1038/s41586-022-04959-9.

Friedlingstein, P., Jones, M.W., O'Sullivan, M., Andrew, R.M., Bakker, D.C.E., Hauck, J., Le Quéré, C., Peters, G.P., Peters, W., Pongratz, J., Sitch, S., Canadell, J.G., Ciais, P., Jackson, R.B., Alin, S.R., Anthoni, P., Bates, N.R., Becker, M., Bellouin, N., Bopp, L., Chau, T.T.T., Chevallier, F., Chini, L.P., Cronin, M., Currie, K.I., Decharme, B., Djeutchouang, L.M., Dou, X., Evans, W., Feely, R.A., Feng, L., Gasser, T., Gilfillan, D., Gkritzalis, T., Grassi, G., Gregor, L., Gruber, N., Gürses, Ö., Harris, I., Houghton, R. A., Hurtt, G.C., Iida, Y., Ilyina, T., Luijkx, I.T., Jain, A., Jones, S.D., Kato, E., Kennedy, D., Klein Goldewijk, K., Knauer, J., Korsbakken, J.I., Körtzinger, A., Landschützer, P., Lauvset, S.K., Lefèvre, N., Lienert, S., Liu, J., Marland, G., McGuire, P.C., Melton, J.R., Munro, D.R., Nabel, J.E.M.S., Nakaoka, S.-I., Niwa, Y., Ono, T., Pierrot, D., Poulter, B., Rehder, G., Resplandy, L., Robertson, E., Rödenbeck, C., Rosan, T.M., Schwinger, J., Schwingshackl, C., Séférian, R., Sutton, A.J., Sweeney, C., Tanhua, T., Tans, P.P., Tian, H., Tilbrook, B., Tubiello, F., van der Werf, G.R., Vuichard, N., Wada, C., Wanninkhof, R., Watson, A.J., Willis, D., Wiltshire, A.J., Yuan, W., Yue, C., Yue, X., Zaehle, S., Zeng, J., 2022. Global carbon budget 2021. Earth Syst. Sci. Data 14, 1917–2005. https://doi.org/10.5194/essd-14-1917-2022.

Friedman, J.H., 2001. Greedy function approximation: a gradient boosting machine. Ann. Stat. 29, 1189–1232. https://doi.org/10.1214/aos/1013203451.

Gampe, D., Zscheischler, J., Reichstein, M., O'Sullivan, M., Smith, W.K., Sitch, S., Buermann, W., 2021. Increasing impact of warm droughts on northern ecosystem productivity over recent decades. Nat. Clim. Chang. 11, 772–779. https://doi.org/10.1038/s41558-021-01112-8.

Gao, J., Barzel, B., Barabási, A.-L., 2016. Universal resilience patterns in complex networks. Nature 530, 307–312. https://doi.org/10.1038/nature16948.

Gao, S., Liang, E., Liu, R., Lu, X., Rossi, S., Zhu, H., Piao, S., Peñuelas, J., Camarero, J.J., 2024. Shifts of forest resilience after seismic disturbances in tectonically active regions. Nat. Geosci. 17, 189–196. https://doi.org/10.1038/s41561-024-01380-x.

Gladstone-Gallagher, R.V., Pilditch, C.A., Stephenson, F., Thrush, S.F., 2019. Linking traits across ecological scales determines functional resilience. Trends Ecol. Evol. 34, 1080–1091. https://doi.org/10.1016/j.tree.2019.07.010.

Green, J.K., Seneviratne, S.I., Berg, A.M., Findell, K.L., Hagemann, S., Lawrence, D.M., Gentine, P., 2019. Large influence of soil moisture on long-term terrestrial carbon uptake. Nature 565, 476–479. https://doi.org/10.1038/s41586-018-0848-x.

Greenwell, M.P., Brereton, T., Day, J.C., Roy, D.B., Oliver, T.H., 2019. Predicting resilience of ecosystem functioning from co-varying species' responses to environmental change. Ecol. Evol. 9, 11775–11790. https://doi.org/10.1002/ece3.5679.

Guo, W., Huang, S., Huang, Q., Leng, G., Mu, Z., Han, Z., Wei, X., She, D., Wang, H., Wang, Z., Peng, J., 2023. Drought trigger thresholds for different levels of vegetation loss in China and their dynamics. Agric. For. Meteorol. 331, 109349. https://doi.org/10.1016/j.agrformet.2023.109349.

Hoek van Dijke, A.J., Herold, M., Mallick, K., Benedict, I., Machwitz, M., Schlerf, M., Pranindita, A., Theeuwen, J.J.E., Bastin, J.-F., Teuling, A.J., 2022. Shifts in regional water availability due to global tree restoration. Nat. Geosci. 15, 363–368. https://doi.org/10.1038/s41561-022-00935-0.

Holling, C.S., 1996. Engineering resilience versus ecological resilience. Eng. Eco. Const. 31–32.

Hong, S., Yin, G., Piao, S., Dybzinski, R., Cong, N., Li, X., Wang, K., Peñuelas, J., Zeng, H., Chen, A., 2020. Divergent responses of soil organic carbon to afforestation. Nat. Sustain. 3, 694–700. https://doi.org/10.1038/s41893-020-0557-y.

Hu, Z., Guo, Q., Li, S., Piao, S., Knapp, A.K., Ciais, P., Li, X., Yu, G., 2018. Shifts in the dynamics of productivity signal ecosystem state transitions at the biome-scale. Ecol. Lett. 21, 1457–1466. https://doi.org/10.1111/ele.13099.

Jiao, W., Wang, L., Smith, W.K., Chang, Q., Wang, H., D'Odorico, P., 2021. Observed increasing water constraint on vegetation growth over the last three decades. Nat. Commun. 12, 3777. https://doi.org/10.1038/s41467-021-24016-9.

Johnson, M., Ballantyne, A., Graham, J., Holden, Z., Hoylman, Z., Jensco, K., Ketchum, D., Kimball, J., Mitchell, J., 2025. An ecosystem resilience index that integrates measures of vegetation function, structure, and composition. Ecol. Ind. 171, 113076. https://doi.org/10.1016/j.ecolind.2025.113076.

Joiner, J., Yoshida, Y., 2020. Satellite-based reflectances capture large fraction of variability in global gross primary production (GPP) at weekly time scales. Agric. For. Meteorol. 291, 108092. https://doi.org/10.1016/j.agrformet.2020.108092.

Kéfi, S., Dakos, V., Scheffer, M., Van Nes, E.H., Rietkerk, M., 2013. Early warning signals also precede non-catastrophic transitions. Oikos 122, 641–648. https://doi.org/10.1111/j.1600-0706.2012.20838.x.

Keith, D.A., Benson, D.H., Baird, I.R.C., Watts, L., Simpson, C.C., Krogh, M., Gorissen, S., Ferrer-Paris, J.R., Mason, T.J., 2023. Effects of interactions between anthropogenic stressors and recurring perturbations on ecosystem resilience and collapse. Conserv. Biol. 37, e13995. https://doi.org/10.1111/cobi.13995.

Lenton, T.M., Abrams, J.F., Bartsch, A., Bathiany, S., Boulton, C.A., Buxton, J.E., Conversi, A., Cunliffe, A.M., Hebden, S., Lavergne, T., Poulter, B., Shepherd, A., Smith, T., Swingedouw, D., Winkelmann, R., Boers, N., 2024. Remotely sensing potential climate change tipping points across scales. Nat. Commun. 15, 343. https://doi.org/10.1038/s41467-023-44609-w.

Li, X., Piao, S., Huntingford, C., Peñuelas, J., Yang, H., Xu, H., Chen, A., Friedlingstein, P., Keenan, T.F., Sitch, S., Wang, X., Zscheischler, J., Mahecha, M.D., 2023. Global variations in critical drought thresholds that impact vegetation. Natl. Sci. Rev. 10, nwad049. https://doi.org/10.1093/nsr/nwad049.

Li, X., Piao, S., Wang, K., Wang, X., Wang, T., Ciais, P., Chen, A., Lian, X., Peng, S., Peñuelas, J., 2020. Temporal trade-off between gymnosperm resistance and resilience increases forest sensitivity to extreme drought. Nat. Ecol. Evol. 4, 1075–1083. https://doi.org/10.1038/s41559-020-1217-3.

Lipoma, L., Kambach, S., Díaz, S., Sabatini, F.M., Damasceno, G., Kattge, J., Wirth, C., Abella, S.R., Beierkuhnlein, C., Belote, T.R., Bernhardt-Römermann, M., Craven, D., Dolezal, J., Eisenhauer, N., Isbell, F., Jentsch, A., Kreyling, J., Lanta, V., Le Stradic, S., Lepš, J., Manninen, O., Mariotte, P., Reich, P.B., Ruppert, J.C., Schmidt, W., Tilman, D., van Ruijven, J., Wagg, C., Wardle, D.A., Wilsey, B., Bruelheide, H., 2024. No general support for functional diversity enhancing resilience across terrestrial plant communities. Glob. Ecol. Biogeogr. 33, e13895. https://doi.org/10.1111/geb.13895.

Liu, M., Trugman, A.T., Peñuelas, J., Anderegg, W.R.L., 2024. Climate-driven disturbances amplify forest drought sensitivity. Nat. Clim. Chang. 1–7. https://doi.org/10.1038/s41558-024-02022-1.

Liu, T., Chen, D., Yang, L., Meng, J., Wang, Z., Ludescher, J., Fan, J., Yang, S., Chen, D., Kurths, J., Chen, X., Havlin, S., Schellnhuber, H.J., 2023. Teleconnections among tipping elements in the Earth system. Nat. Clim. Chang. 13, 67–74. https://doi.org/10.1038/s41558-022-01558-4.

Lohmann, J., Dijkstra, H.A., Jochum, M., Lucarini, V., Ditlevsen, P.D., 2024. Multistability and intermediate tipping of the Atlantic Ocean circulation. Sci. Adv. 10, eadi4253. https://doi.org/10.1126/sciadv.adi4253.

McDowell, N.G., Allen, C.D., Anderson-Teixeira, K., Aukema, B.H., Bond-Lamberty, B., Chini, L., Clark, J.S., Dietze, M., Grossiord, C., Hanbury-Brown, A., Hurtt, G.C., Jackson, R.B., Johnson, D.J., Kueppers, L., Lichstein, J.W., Ogle, K., Poulter, B., Pugh, T.A.M., Seidl, R., Turner, M.G., Uriarte, M., Walker, A.P., Xu, C., 2020. Pervasive shifts in forest dynamics in a changing world. Science 368, eaaz9463. https://doi.org/10.1126/science.aaz9463.

Merganičová, K., Merganič, J., Lehtonen, A., Vacchiano, G., Sever, M.Z.O., Augustynczik, A.L.D., Grote, R., Kyselová, I., Mäkelä, A., Yousefpour, R., Krejza, J., Collalti, A., Reyer, C.P.O., 2019. Forest carbon allocation modelling under climate change. Tree Physiol. 39, 1937–1960. https://doi.org/10.1093/treephys/tpz105.

Meyer, K., Hoyer-Leitzel, A., Iams, S., Klasky, I., Lee, V., Ligtenberg, S., Bussmann, E., Zeeman, M.L., 2018. Quantifying resilience to recurrent ecosystem disturbances using flow–kick dynamics. Nat. Sustain. 1, 671–678. https://doi.org/10.1038/s41893-018-0168-z.

Niu, T., Hou, Z., Yu, J., Zhao, C., Liu, Y., Zuo, X., Zhang, Z., Li, Z., Wang, Y., 2025. Interactions between the structure of forest-grassland ecological spatial networks and water conservation functions at a national scale. Landsc. Archit. Sustain. 1, 100004. https://doi.org/10.1016/j.las.2025.100004.

Oliver, T.H., Heard, M.S., Isaac, N.J.B., Roy, D.B., Procter, D., Eigenbrod, F., Freckleton, R., Hector, A., Orme, C.D.L., Petchey, O.L., Proença, V., Raffaelli, D., Suttle, K.B., Mace, G.M., Martín-López, B., Woodcock, B.A., Bullock, J.M., 2015. Biodiversity and resilience of ecosystem functions. Trends Ecol. Evol. 30, 673–684. https://doi.org/10.1016/j.tree.2015.08.009.

Pan, Y., Birdsey, R.A., Fang, J., Houghton, R., Kauppi, P.E., Kurz, W.A., Phillips, O.L., Shvidenko, A., Lewis, S.L., Canadell, J.G., Ciais, P., Jackson, R.B., Pacala, S.W., McGuire, A.D., Piao, S., Rautiainen, A., Sitch, S., Hayes, D., 2011. A Large and Persistent Carbon Sink in the World's Forests. Science 333, 988–993. https://doi.org/10.1126/science.1201609.

Piao, S., Fang, J., Zhu, B., Tan, K., 2005. Forest biomass carbon stocks in China over the past 2 decades: Estimation based on integrated inventory and satellite data. J. Geophys. Res. Biogeosci. 110, G01006. https://doi.org/10.1029/2005JG000014.

Poorter, L., Bongers, F., Aide, T.M., Almeyda Zambrano, A.M., Balvanera, P., Becknell, J. M., Boukili, V., Brancalion, P.H.S., Broadbent, E.N., Chazdon, R.L., Craven, D., de Almeida-Cortez, J.S., Cabral, G.A.L., de Jong, B.H.J., Denslow, J.S., Dent, D.H., DeWalt, S.J., Dupuy, J.M., Durán, S.M., Espírito-Santo, M.M., Fandino, M.C., César, R.G., Hall, J.S., Hernandez-Stefanoni, J.L., Jakovac, C.C., Junqueira, A.B., Kennard, D., Letcher, S.G., Licona, J.-C., Lohbeck, M., Marín-Spiotta, E., Martínez-Ramos, M., Massoca, P., Meave, J.A., Mesquita, R., Mora, F., Muñoz, R., Muscarella, R., Nunes, Y.R.F., Ochoa-Gaona, S., de Oliveira, A.A., Orihuela-Belmonte, E., Peña-Claros, M., Pérez-García, E.A., Piotto, D., Powers, J.S., Rodríguez-Velázquez, J., Romero-Pérez, I.E., Ruíz, J., Saldarriaga, J.G., Sanchez-Azofeifa, A., Schwartz, N.B., Steininger, M.K., Swenson, N.G., Toledo, M., Uriarte, M., van Breugel, M., van der Wal, H., Veloso, M.D.M., Vester, H.F.M., Vicentini, A., Vieira, I. C.G., Bentos, T.V., Williamson, G.B., Rozendaal, D.M.A., 2016. Biomass resilience of Neotropical secondary forests. Nature 530, 211–214. https://doi.org/10.1038/nature16512.

Reid, W.V., Mooney, H.A., Cropper, A., Capistrano, D., Carpenter, S.R., Chopra, K., Dasgupta, P., Dietz, T., Duraiappah, A.K., Hassan, R., Kasperson, R., Leemans, R., May, R.M., McMichael, A.J., Pingali, P., Samper, C., Scholes, R., Watson, R.T., Zakri, A.H., Shidong, Z., Ash, N.J., Bennett, E., Kumar, P., Lee, M.J., Raudsepp-Hearne, C., Simons, H., Thonell, J., Zurek, M.B., 2005. Ecosystems and human well-being: Synthesis. a report of the Millennium Ecosystem Assessment. Island Press, Washington, DC.

Rietkerk, M., Bastiaansen, R., Banerjee, S., van de Koppel, J., Baudena, M., Doelman, A., 2021. Evasion of tipping in complex systems through spatial pattern formation. Science 374, eabj0359. https://doi.org/10.1126/science.abj0359.

Sanchez-Martinez, P., Martius, L.R., Bittencourt, P., Silva, M., Binks, O., Coughlin, I., Negrão-Rodrigues, V., Athaydes Silva, J., Da Costa, A.C.L., Selman, R., Rifai, S., Rowland, L., Mencuccini, M., Meir, P., 2025. Amazon rainforest adjusts to long-term experimental drought. Nat. Ecol. Evol. 9, 970–979. https://doi.org/10.1038/s41559-025-02702-x.

Scheffer, M., Bascompte, J., Brock, W.A., Brovkin, V., Carpenter, S.R., Dakos, V., Held, H., Van Nes, E.H., Rietkerk, M., Sugihara, G., 2009. Early-warning signals for critical transitions. Nature 461, 53–59. https://doi.org/10.1038/nature08227.

Scheffer, M., Carpenter, S., Foley, J.A., Folke, C., Walker, B., 2001. Catastrophic shifts in ecosystems. Nature 413, 591–596. https://doi.org/10.1038/35098000.

Scheffer, M., Carpenter, S.R., 2003. Catastrophic regime shifts in ecosystems: linking theory to observation. Trends Ecol. Evol. 18, 648–656. https://doi.org/10.1016/j.tree.2003.09.002.

Seddon, A.W.R., Macias-Fauria, M., Long, P.R., Benz, D., Willis, K.J., 2016. Sensitivity of global terrestrial ecosystems to climate variability. Nature 531, 229–232. https://doi.org/10.1038/nature16986.

Seidl, R., Thom, D., Kautz, M., Martin-Benito, D., Peltoniemi, M., Vacchiano, G., Wild, J., Ascoli, D., Petr, M., Honkaniemi, J., Lexer, M.J., Trotsiuk, V., Mairota, P., Svoboda, M., Fabrika, M., Nagel, T.A., Reyer, C.P.O., 2017. Forest disturbances under climate change. Nat. Clim. Chang. 7, 395–402. https://doi.org/10.1038/nclimate3303.

Senf, C., Buras, A., Zang, C.S., Rammig, A., Seidl, R., 2020. Excess forest mortality is consistently linked to drought across Europe. Nat. Commun. 11, 6200. https://doi.org/10.1038/s41467-020-19924-1.

Smith, T., Traxl, D., Boers, N., 2022. Empirical evidence for recent global shifts in vegetation resilience. Nat. Clim. Chang. 12, 477–484. https://doi.org/10.1038/s41558-022-01352-2.

Smith, T., Boers, N., 2023a. Reliability of vegetation resilience estimates depends on biomass density. Nat. Ecol. Evol. 7, 1799–1808. https://doi.org/10.1038/s41559-023-02194-7.

Smith, T., Boers, N., 2023b. Global vegetation resilience linked to water availability and variability. Nat. Commun. 14, 498. https://doi.org/10.1038/s41467-023-36207-7.

Smith, T., Zotta, R.-M., Boulton, C.A., Lenton, T.M., Dorigo, W., Boers, N., 2023. Reliability of resilience estimation based on multi-instrument time series. Earth Syst. Dyn. 14, 173–183. https://doi.org/10.5194/esd-14-173-2023.

Walker, B., Holling, C.S., Carpenter, S., Kinzig, A., 2004. Resilience, adaptability and transformability in social–ecological systems. Ecol. Soc. 9, 5. https://doi.org/10.5751/ES-00650-090205.

Wang, Q., Zeng, J., Qi, J., Zhang, X., Zeng, Y., Shui, W., Xu, Z., Zhang, R., Wu, X., Cong, J., 2021a. A multi-scale daily SPEI dataset for drought characterization at observation stations over mainland China from 1961 to 2018. Earth Syst. Sci. Data 13, 331–341. https://doi.org/10.5194/essd-13-331-2021.

Wang, S., Zhang, Y., Ju, W., Qiu, B., Zhang, Z., 2021b. Tracking the seasonal and inter-annual variations of global gross primary production during last four decades using satellite near-infrared reflectance data. Sci. Total Environ. 755, 142569. https://doi.org/10.1016/j.scitotenv.2020.142569.

Xu, Q., Yu, R., Guo, L., 2024. Evaluation of forest ecosystem resilience to drought considering lagged effects of drought. Ecol. Evol. 14, e70281. https://doi.org/10.1002/ece3.70281.

Yan, Y., Hong, S., Chen, A., Peñuelas, J., Allen, C.D., Hammond, W.M., Munson, S.M., Myneni, R.B., Piao, S., 2025. Satellite-based evidence of recent decline in global forest recovery rate from tree mortality events. Nat. Plants 11, 731–742. https://doi.org/10.1038/s41477-025-01948-4.

Yang, J., Huang, X., 2021. The 30 m annual land cover dataset and its dynamics in China from 1990 to 2019. Earth Syst. Sci. Data 13, 3907–3925. https://doi.org/10.5194/essd-13-3907-2021.

Zaitchik, B.F., Rodell, M., Biasutti, M., Seneviratne, S.I., 2023. Wetting and drying trends under climate change. Nat. Water 1, 502–513. https://doi.org/10.1038/s44221-023-00073-w.

Zhao, M., Heinsch, F.A., Nemani, R.R., Running, S.W., 2005. Improvements of the MODIS terrestrial gross and net primary production global data set. Remote Sens. Environ. 95, 164–176. https://doi.org/10.1016/j.rse.2004.12.011.

Zheng, Y., Shen, R., Wang, Y., Li, X., Liu, S., Liang, S., Chen, J.M., Ju, W., Zhang, L., Yuan, W., 2020. Improved estimate of global gross primary production for reproducing its long-term variation, 1982–2017. Earth Syst. Sci. Data 12, 2725–2746. https://doi.org/10.5194/essd-12-2725-2020.